CHEMISTRY

A EUROPEAN JOURNAL

Supporting Information

Multinuclear Solid-State Magnetic Resonance as a Sensitive Probe of Structural Changes upon the Occurrence of Halogen Bonding in Co-crystals

Cory M. Widdifield,[a, c] Gabriella Cavallo,[b] Glenn A. Facey,[a] Tullio Pilati,[b] Jingxiang Lin,[b] Pierangelo Metrangolo,*[b] Giuseppe Resnati,*[b] and David L. Bryce*[a]

chem_201300809_sm_miscellaneous_information.pdf

Table of Contents

X-ray Crystallography – Additional Details

Crystallographic data were collected on a Bruker APEX-II CCD diffractometer, with Mo*K*α radiation (λ = 0.71073 Å). **P2** and **P4** diffracted poorly, with diffuse strikes indicating extended disorder. Attempts to collect data at low temperature failed: the compounds present a phase transition near room temperature and, when cooled, the crystals tend to crumble and to give split diffracted spots that are impossible to integrate correctly. A similar behaviour was found also for **P3**, but at lower temperature: we were able to collect its data at 223 K. The data collection temperature was controlled by a Bruker KRIOFLEX device. The structures were solved using *SIR2002*.[1] **P3** was refined with *SHELX-97*,[2] with non-H atoms anisotropic, while H atoms were treated isotropically and refined with restraints on C-H and H-C-H distances and angles; **P2** and **P4** were refined using *SHELXL-2012* (Sheldrick, G. M. (2012). Univ. of Göttingen, Germany); all atoms were refined anisotropically excluding H atoms, which were placed in calculated positions. The disordered benzene atoms, split in two models, were refined with restraints on their geometry and ADPs.

Table S1. Crystallographic data for the isomorphous structures **P2**, **P3**, and **P4**.

Salt	**P2**	**P3**	**P4**
Formula	$C_{22}H_{38}F_4I_4N_2$	$C_{22}H_{42}I_4N_2$	$C_{22}H_{38}F_4Br_4N_2$
Space group	*C*2/m	*C*2/m	*C*2/m
a [Å]	35.117(11)	29.382(3)	34.226(3)
b [Å]	7.678(2)	7.4019(7)	7.6236(5)
c [Å]	5.873(2)	6.8939(8)	5.9906(5)
β[°]	96.77(2)	90.113(5)	98.570(4)
V [Å^3]	1572.5(8)	1499.3(3)	1545.6(2)
T [K]	room temp.	223(2)	room temp.
D_{calc}	1.931	1.865	1.762
μ[mm^{-1}]	3.999	4.167	4.656
Tmin/Tmax coefficients	0.691/1.000	0.363/0.566	0.223/0.653
θ max/full [°]	26.02/25.24	33.19/25.00	31.65/25.24
θ full completeness.[%]	99.9	99.6	99.7
No. reflections collected	7141	9197	15249
R_{ave}	0.0235	0.0502	0.0184
Independent reflections	1675	2681	2653
Observed [$I>2\sigma$(I)]	1486	2214	1919
Refined parameters	112	127	104
Restraints	89	21	62
R1 (all)	0.0378	0.0366	0.0721
R1 [$I>2\sigma(I)$]	0.0336	0.0286	0.0508
wR2 (all)	0.0947	0. 0739	0.1757
wR2 [$I>2\sigma(I)$]	0.0916	0.0709	0.1536
G.O.F. on F^2		1.052	1.026
$\Delta\rho$ max [eÅ^{-3}]	0.84	1.18	1.66
$\Delta\rho$ min [eÅ^{-3}]	-0.88	-0.72	-1.03
CCDC No.	926827	926828	926829

Additional Experimental and Discussion.

SIMPSON programming details. For ^{14}N MAS SSNMR spectra which were acquired with the variable-offset cumulative spectrum (VOCS)[3-5] method (i.e., **1a·2H$_2$O** and **2a·2H$_2$O**), SIMPSON[6] numerical simulations were performed assuming uniform excitation conditions and hence the effects of finite pulse lengths were not included. For these systems, additional programming details were as follows: number of γ angles = 50; the crystal file was *zcw1596* (larger powder averaging was not found to be necessary); the start and detect operators were I_{1x} and I_{1p}, respectively; the '*gcompute*' method was chosen. The effects of slight off-MAS conditions (up to 0.1°) were tested; however, they did not produce significantly different results. For all other samples for which we recorded ^{14}N MAS NMR spectra (i.e., **P1** – **P5**), they were acquired using a single rf transmitter setting and hence the effects of finite pulse lengths, field strengths, and echo delays were included in the SIMPSON simulations. The effect of including the finite pulses was not dramatic, but generally improved the agreement between the best-fit SIMPSON simulations and the experimental spectra. For this set of simulations: γ angles = 20; the crystal file was *zcw1596*; the start and detect operators were I_{1z} and I_{1p}, respectively. The rf field strength used in the simulations ranged between 32 – 44 kHz (to be in agreement with the actual experiment), the free evolution period (i.e., time-independent Hamiltonian length) was set as 0.4 μs, and coherence selection was explicitly performed for the 0 → +1 → −1 pathway. For all SIMPSON computations, after the calculation, the time-domain response was zero-filled to 8192 points and 70 – 130 Hz of exponential line broadening was used.

Details for generation of ^{13}C-$^{79/81}$Br residual dipolar coupling simulations in Figure S5. The interesting features in the ^{13}C NMR spectra for sample **4b** acquired at B_0 = 9.4 T and 11.75 T (Figure S5c-d), notably in the region extending from 80 – 125 ppm, prompted us to consider the

possibility of residual dipolar coupling (RDC) between the ^{13}C nucleus which is directly bonded to $^{79/81}$Br nuclei. The observation of RDC between carbon and bromine is not unheard of;[7] however, it is uncommon due to the excessive NMR line shape broadening which manifests as a result of this interaction at the ^{13}C site. Remedies to RDC-based line broadening are found simply by performing NMR experiments at higher applied magnetic fields.

Under most physically relevant situations, eight parameters are in theory are required to be specified to fit each unique spin pair experiencing a RDC (i.e., δ_{iso}, C_Q, η_Q, as well as the effective dipolar coupling constant, D_{eff}, the isotropic J-coupling constant, J_{iso}, the anisotropy in the J-tensor, ΔJ, and the two polar angles which relate the electric-field gradient (EFG) principal axis system with that of the dipolar tensor, α_{RDC} and β_{RDC}). The parameter space was greatly restricted, however, by acquiring ^{13}C NMR data at two applied fields, using certain known physical data (such as the ratio between the nuclear quadrupole moments of the ^{79}Br and ^{81}Br nuclei) and by using modern DFT calculations. For more details, those interested are referred to a recent literature account.[8]

In the specific case of the *p*-dibromotetrafluorobenzene molecule, **4b**, we began attempts at a fit of the observed ^{13}C NMR line shapes by estimating the $C_Q(^{79/81}Br)$ and η_Q values for **4b**, initially based upon the known $C_Q(^{79/81}Br)$ and η_Q values for *p*-dibromobenzene: $C_Q(^{79}Br)$ = 535.19 MHz; $C_Q(^{81}Br)$ = 447.4 MHz and η_Q of ca. 0.05.[9-11] Although NQR experiments would have been very relevant in this situation, due to the very high expected resonance frequencies of the NQR transitions, they could not be measured experimentally by us and we instead relied upon a computational approach to constrain the $^{79/81}$Br EFG tensor parameters. To estimate the precision of our computational approach at calculating the bromine EFG tensor parameters for **4b**, we performed gas-phase geometry optimizations of *p*-dibromobenzene and **4b**, followed by

EFG tensor calculations and compared the calculated and experimental values for *p*-dibromobenzene. These calculations were performed rather similarly to the other cluster-based calculations in this manuscript: the version 2012.01 of the ADF software[12-14] was used and relativistic effects were included using the ZORA[15] and included spin-orbit effects. The large QZ4P basis set was used throughout. The only significant change between the present set of calculations and those outlined in the main paper is the use of the meta-GGA exchange-correlation functional of Tao, Perdew, Staroverov, and Scuseria (TPSS),[16,17] which has been demonstrated to be more accurate than regular GGA functionals in many property calculations,[18] and recently illustrated rather convincingly for the calculation of EFG tensors for several quadrupolar nuclei (including $^{79/81}$Br).[19] We chose gas-phase geometry optimizations because even though the crystal structure for *p*-dibromobenzene is known,[20] and while reports of the unit cell measurements are known for **4b**,[21] the atomic positions reported for the structure of **4b** seem to be in error and result in a uncharacteristically short C-Br bond distance of 1.81(1) Å, compared to the accepted value of 1.9 Å.

The DFT-optimized C-Br internuclear distance for an isolated *p*-dibromobenzene molecule was calculated to be 1.908 Å, while the same parameter for **4b** is calculated to be 1.881 Å, which are reasonable values based on the accepted value of 1.9 Å indicated above. Notably, the calculations point to a slight contraction in the C-Br distance in **4b**, which should give rise to an increase in the bromine C_Q value in **4b** relative to *p*-dibromobenzene, if one assumes that the largest component of the EFG tensor, V_{33}, points along the C-Br internuclear vector. Quantum-chemical calculations can determine this orientation, and we calculated here that V_{33} (as expected) points essentially along the C-Br internuclear vector ($\angle$(C-Br-V_{33}) = 0.2°). Knowledge of this allows us to simultaneously constrain $\alpha_{RDC} = \beta_{RDC} = 0°$. With regards to the

computed EFG tensor parameters for the gas-phase optimized structures of *p*-dibromobenzene and **4b**, we begin by stating that the calculated values for *p*-dibromobenzene are: $C_Q(^{79}Br)$ = −584.23 MHz; $C_Q(^{79}Br)$ = −488.86 MHz; and η_Q = 0.0768. We see therefore that the computational model overestimates the EFG tensor magnitude of *p*-dibromobenzene by roughly 9%, which is to be expected as both intermolecular and temperature effects are not included in the computation. We assume that this same overestimation applies equally well to **4b**, where it is calculated that $C_Q(^{79}Br)$ = −658.28 MHz, $C_Q(^{79}Br)$ = −550.86 MHz, and η_Q = 0.1145. We also note that the negative C_Q values are consistent with the experimental data, as attempts to fit the ^{13}C NMR line shapes of **4b** with positive bromine C_Q values were very unsatisfactory. From the DFT-optimized structure, we can easily estimate an upper bound for the dipolar coupling constant, *D*, which will later be subjected to some small corrections (hence yielding D_{eff}). As the ^{79}Br and ^{81}Br nuclei each possess a unique magnetogyric ratio, γ, each *D* value will therefore be slightly different depending on the spin pair. Neglecting isotope-dependent bond length changes in **4b**, we calculate *D* = 1141 Hz for the ^{13}C-^{79}Br spin pair, and 1230 Hz for the ^{13}C-^{81}Br spin pair. We note here that the experimental *D* value is a motionally averaged property, while the computed structure is static. We also note that the value of the motionally averaged *D* value requires a scaling that depends on ΔJ (explicitly, $D_{eff} = D - \Delta J/3$). This naturally leads us to a brief discussion of *J*-coupling constants for the ^{13}C-^{79}Br and ^{13}C-^{81}Br spin pairs in **4b**.

The *J* tensor was calculated explicitly for the ^{13}C-^{79}Br spin pair using the CPL module[22-27] which is included within the ADF software suite. The PBE GGA exchange correlation functional outlined in the main paper was used (meta-GGA functionals are noted by the developer as being not reliable presently) and finite nuclear effects were included by approximating the nuclei with a Gaussian charge distribution.[28] The 'jcpl' basis sets developed

recently for *J* tensor computations within the ZORA were used.[29,30] Self-consistent field (SCF) convergence was set to be very tight (1.0e-8) and all relevant mechanisms which contribute to the *J* coupling tensor were considered (i.e., Fermi-contact, spin-dipolar, paramagnetic spin-orbit and diamagnetic spin-orbit, including relevant cross terms). The resulting *J* tensor eigenvalues for **4b** (^{13}C-^{79}Br spin pair) were computed to be: J_{11} = −265.1 Hz; J_{22} = −254.6 Hz; and J_{33} = −129.3 Hz. This leads to J_{iso} = −216.4 Hz and ΔJ = 130.5 Hz. Similar parameters for the ^{13}C-^{81}Br spin pair also exist: J_{iso} = −233.2 Hz; ΔJ = 140.7 Hz. This allows us to establish approximate values for D_{eff} for each spin pair: 1097 Hz for ^{13}C-^{79}Br and 1183 Hz for ^{13}C-^{81}Br. At this point, all parameters except δ_{iso} have been reasonably established and we keep the chemical shift as the free parameter. After reducing the calculated bromine-79/81 EFG tensor magnitudes by 9% (leading to C_Q(^{79}Br) = 599 MHz and C_Q(^{81}Br) = 501 MHz for **4b**) and adding a chemical shift of 100.5(1.0) ppm, satisfactory fits of the ^{13}C NMR data for **4b** at both applied fields are reached, as shown in Figure S5c-d. We did not attempt any additional line shape fitting due to the very large parameter space and note that this is a preliminary finding. At the same time, we believe the intended objective (i.e., demonstrating that the 'interesting' line shape of the ^{13}C NMR spectrum of **4b** is due to RDC between ^{13}C and $^{79/81}$Br) has been conclusively achieved. Future $^{79/81}$Br NQR measurements could greatly enhance the confidence in these preliminary values, but this is beyond the scope of our present study.

Table S2. Detailed ^{13}C SSNMR experimental acquisition parameters[a]

compound	B_0 / T	window / kHz	ν_{MAS} / kHz	points[b]	$\pi/2$ / μs[c]	contact time / ms	Scans	recycle delay / s	details
1a·2H$_2$O	11.75	66.67	5.0	4096	3.75	5.0	3586	1.5	RAMP-CP from ^1H
2a·2H$_2$O	11.75	66.67	5.0	4096	3.75	5.0	18480	3.0	RAMP-CP from ^1H
2b	9.4	50.0	12.0	1358	2.50	—	3440	20.0	Hahn echo using direct ^{13}C polarization; no decoupling; rotor-synchronized data acquisition
3b	9.4	50.0	7.0	1994	3.20	2.0	780	5.0	RAMP-CP from ^1H; SPINAL-64[31] decoupling
4b	9.4	50.0	12.0	1494	2.50	—	4512	20.0	Hahn echo using direct ^{13}C polarization; no decoupling; rotor-synchronized data acquisition
	11.75	62.89	10.0	1024	3.00	—	657	20.0	Bloch decay using direct ^{13}C polarization
P1	11.75	66.67	5.0	4096	3.75	5.0	3216	3.0	RAMP-CP from ^1H
P2	9.4	50.0	6.5	4994	3.20	5.0	2752	1.5	RAMP-CP from ^1H
P3	9.4	50.0	6.2	5994	3.20	5.0	1024	1.5	RAMP-CP from ^1H
P4	11.75	62.89	10.0	5120	3.00	2.0	25933	2.0	RAMP-CP from ^1H, T = room temp.
P5	11.75	66.67	5.0	4096	3.75	5.0	15840	3.0	RAMP-CP from ^1H

[a] Unless denoted otherwise, experiments used a 4 mm HXY MAS probe, were performed at T = 285.0(0.2) K, and used two pulse phase modulated (TPPM)[32] decoupling of the ^1H nuclei during acquisition (ν_{TPPM} or ν_{SPINAL} > 65 kHz).
[b] Complex time-domain data points.
[c] Corresponds to the $\pi/2$ ^1H pulse length used, except for experiments upon compounds **2b** and **4b**, where it corresponds to the $\pi/2$ ^{13}C pulse length used.

Table S3. Detailed ^{15}N SSNMR experimental acquisition parameters[a]

compound	B_0 / T	window / kHz	ν_{MAS} / kHz	points[b]	$\pi/2$ / μs[c]	contact time / ms	scans	ν_{TPPM} / kHz	recycle delay / s	details
1a·2H$_2$O	11.75	10.0	5.0	1498	5.0	8.0	7840	25.0	1.5	4mm HX MAS probe; T = 285 K
	11.75	10.0	static	1024	5.0	8.0	43408	25.0	1.5	4mm HX MAS probe; T = 292 K
2a·2H$_2$O	9.4	25.0	5.0	2048	3.0	5.0	7104	35.2	1.0	4mm HXY MAS probe; T = 293 K
	9.4	25.0	static	4096	3.0	5.0	38597	35.2	1.0	4mm HXY MAS probe; T = 293 K
P1	11.75	10.0	5.0	1498	5.0	8.0	5664	25.0	1.5	4mm HX MAS probe; T = 285 K
	11.75	10.0	static	1024	5.0	8.0	43792	25.0	1.5	4mm HX MAS probe; T = 292 K
P2	9.4	20.0	5.0	3196	3.0	5.0	3808	49.6	1.5	4mm HXY MAS probe; T = 285 K
	9.4	20.0	static	1196	3.0	5.0	33168	49.6	1.5	4mm HXY MAS probe; T = 292 K
P3	9.4	20.0	5.0	3998	3.0	5.0	2736	49.6	1.5	4mm HXY MAS probe; T = 285 K
P4	11.75	30.3	4.0	3072	7.0	8.0	9616	35.7	2.0	4mm HX MAS probe; T = room temp.
P5	9.4	25.0	5.0	4096	3.0	5.0	47601	35.2	1.0	4mm HXY MAS probe; T = 293 K

[a] Unless denoted otherwise, RAMP-CP experiments were used, and employed TPPM[32] decoupling of the ^{1}H nuclei during acquisition.
[b] Complex time-domain data points.
[c] Corresponds to the $\pi/2$ ^{1}H pulse length used.

Table S4. Detailed ^{14}N SSNMR experimental acquisition parameters[a]

compound	B_0 / T	window / kHz	ν_{MAS} / kHz	points[b]	$\pi/2$ / μs	scans[c]	recycle delay / s	details
1a·2H$_2$O	11.75	400	8.0	8192	7.0	11910	5.0	VOCS data acquisition with 3 pieces; offset = 40 kHz; continuous wave (CW) ^{1}H decoupling tested (ν_{CW} = 28.1 kHz)
2a·2H$_2$O	11.75	400	8.0	8192	7.0	2000	5.0	T = room temperature; VOCS data acquisition with 3 pieces; offset = 100 kHz
P1	11.75	400	4.0	8192	7.0	37712	2.0	—
P2	11.75	400	4.0	39958	7.0	21744	2.0	CW ^{1}H decoupling tested (ν_{CW} = 31.6 kHz)
P3	11.75	400	4.0	39958	8.0	15808	2.0	CW ^{1}H decoupling tested (ν_{CW} = 31.6 kHz)
P4	11.75	400	4.0	39958	5.6	10000	2.0	CW ^{1}H decoupling tested (ν_{CW} = 44.6 kHz), T = room temp.
P5	11.75	400	4.0	8192	7.0	15180	5.0	—

[a] Unless denoted otherwise, a 4 mm HX MAS probe was used with a rotor-synchronized echo pulse sequence[33] and T = 285 K.
[b] Complex time-domain data points.
[c] For NMR spectra which were acquired using the VOCS method, this corresponds to the number of scans per each individual sub-spectrum.

Table S5. Detailed ^{127}I SSNMR experimental acquisition parameters[a]

compound	B_0 / T	window / kHz	points[b]	$\pi/2$ / μs	τ / μs	scans	recycle delay / s	details
1a·2H$_2$O	9.4	2000	1024	1.0	29.0	32768	0.25	4 mm HXY MAS probe; VOCS data acquisition: 10 pieces with uniform offset of 250 kHz; CW ^{1}H decoupling tested (ν_{CW} ~ 73.5 kHz). Preliminary spectrum.
	21.1	2000	1024	1.4	18.6	6000	0.25	5 mm home-built static HX probe; VOCS data acquisition: 7 pieces with uniform offset of 250 kHz; CW ^{1}H decoupling tested (ν_{CW} ~ 30 kHz)
2a·2H$_2$O	21.1	2000	1024	1.4	18.6	4096	0.25	5 mm home-built static HX probe; VOCS data acquisition: 6 pieces with uniform offset of 250 kHz; CW ^{1}H decoupling tested (ν_{CW} ~ 30 kHz)
P3	11.75	2000	1024	1.0	18.5	27344	0.25	4 mm MAS probe; Hahn echo experiment; VOCS data acquisition: 10 pieces with uniform offset of 250 kHz. Preliminary spectrum.
	21.1	2000	512	1.0	19.0	10000	0.25	4 mm home-built static HX probe; VOCS data acquisition: 8 pieces with uniform offset of 300 kHz; CW ^{1}H decoupling tested (ν_{CW} ~ 40 kHz)

[a] Unless denoted otherwise, for all ^{127}I NMR experiments above, the Solomon echo pulse sequence[33] was used, and spectra were acquired at ambient temperature.
[b] Complex time-domain data points.

Table S6. Detailed ^{19}F SSNMR experimental acquisition parameters[a]

compound	B_0 / T	window / kHz	ν_{MAS} / kHz	points[b]	$\pi/2$ / μs	scans	recycle delay / s	details
2b	9.4	200	12.0	4096	2.75	16	15.0	4 mm HXY MAS probe
4b	9.4	200	12.0	4096	2.75	16	15.0	4 mm HXY MAS probe
P2	4.7	81.521	25.0	1024	2.1	128	5.0	2.5 mm HX MAS probe
P4	4.7	81.521	25.0	1024	2.1	128	5.0	2.5 mm HX MAS probe

[a] For all ^{19}F NMR experiments displayed in the table above, a rotor-synchronized Hahn echo pulse sequence[34] was used, and spectra were acquired at ambient temperature. However, for samples **P2** and **P4**, additional variable temperature NMR experiments were also attempted, and used exactly the same parameters as the ambient temperature experiments indicated in the above table, except that ν_{MAS} = 15 kHz.
[b] Complex time-domain data points.

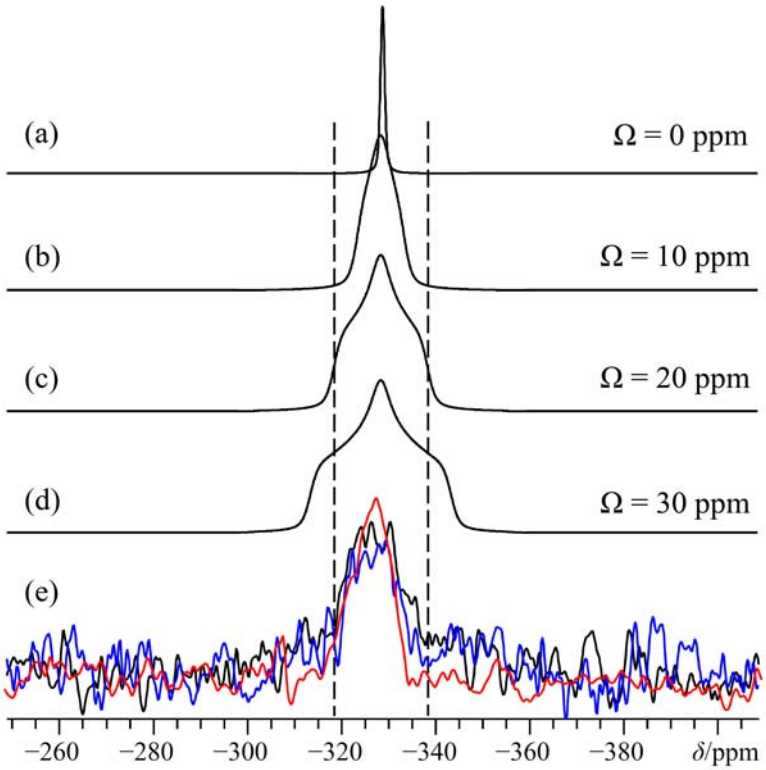

Figure S1. Experimental RAMP-CP/static $^{15}N\{^{1}H\}$ NMR spectra of **1a·2H$_2$O** (e, black trace), **P1** (e, blue trace), and **P2** (e, red trace), as well as analytical WSolids simulations (a – d), which highlight that while the nitrogen CSA is rather small, it is clearly nonzero. Additionally, it is found that the nitrogen CSA does not change markedly upon formation of the supramolecular complex. The span values used in the line shape simulations are provided to the right in (a – d). All simulations assume $\kappa = 0$. Due to the poor signal-to-noise ratio associated with the experimental data, the line shape models are not meant to be quantitative, but to show that $\Omega < 20$ ppm (as further justified in Figure S2). The experimental spectra were acquired at $B_0 = 9.4$ T (e, red trace) and $B_0 = 11.75$ T (e, black and blue traces) and $T = 292$ K.

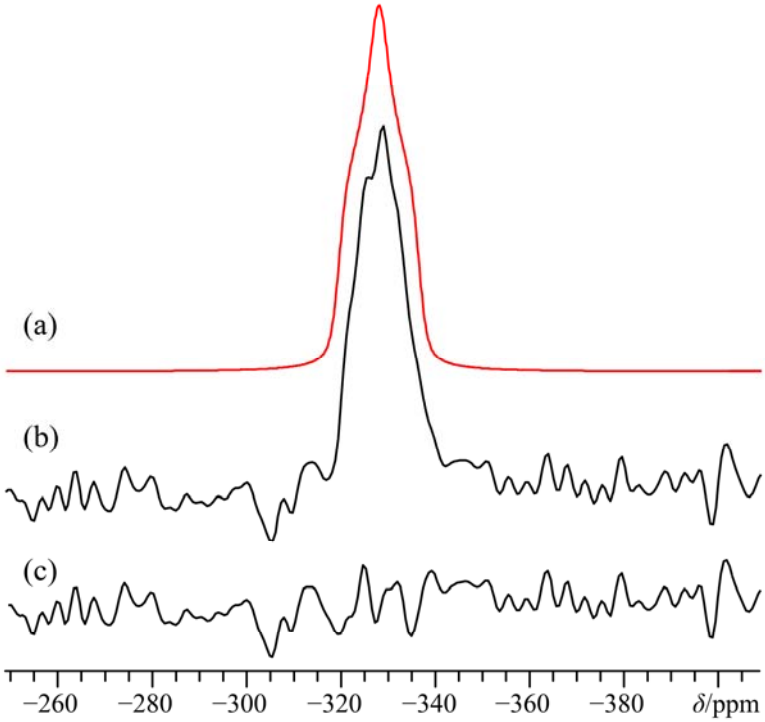

Figure S2. Experimental RAMP-CP/static $^{15}N\{^{1}H\}$ NMR spectrum of **2a·2H$_2$O** (b), an analytical WSolids simulation (a), and a difference spectrum between the experimental and simulated spectra (c). The nitrogen CSA parameters used in the line shape simulation are as follows: Ω = 17 ppm, κ = 0. The experimental spectrum was acquired at B_0 = 9.4 T and T = 293 K.

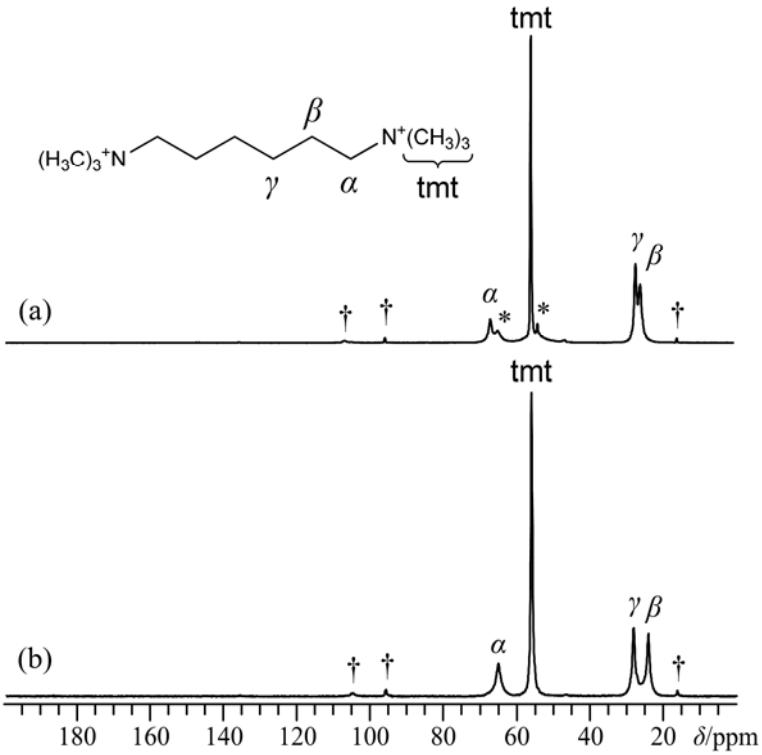

Figure S3. Experimental ^{13}C RAMP-CP/MAS NMR spectra of compounds **2a·2H$_2$O** (a), and **P5** (b). Both complexes include the hexamethonium dication (i.e., $(CH_3)_3N^+(CH_2)_6N^+(CH_3)_3$) in their respective structures. The spectra were acquired at B_0 = 11.75 T, ν_{MAS} = 5 kHz, and T = 285 K. Minor peaks due to MAS spinning sidebands are denoted using daggers. Suspected impurity peaks are specified with asterisks. Assignments are according to the labeling scheme inset above (a).

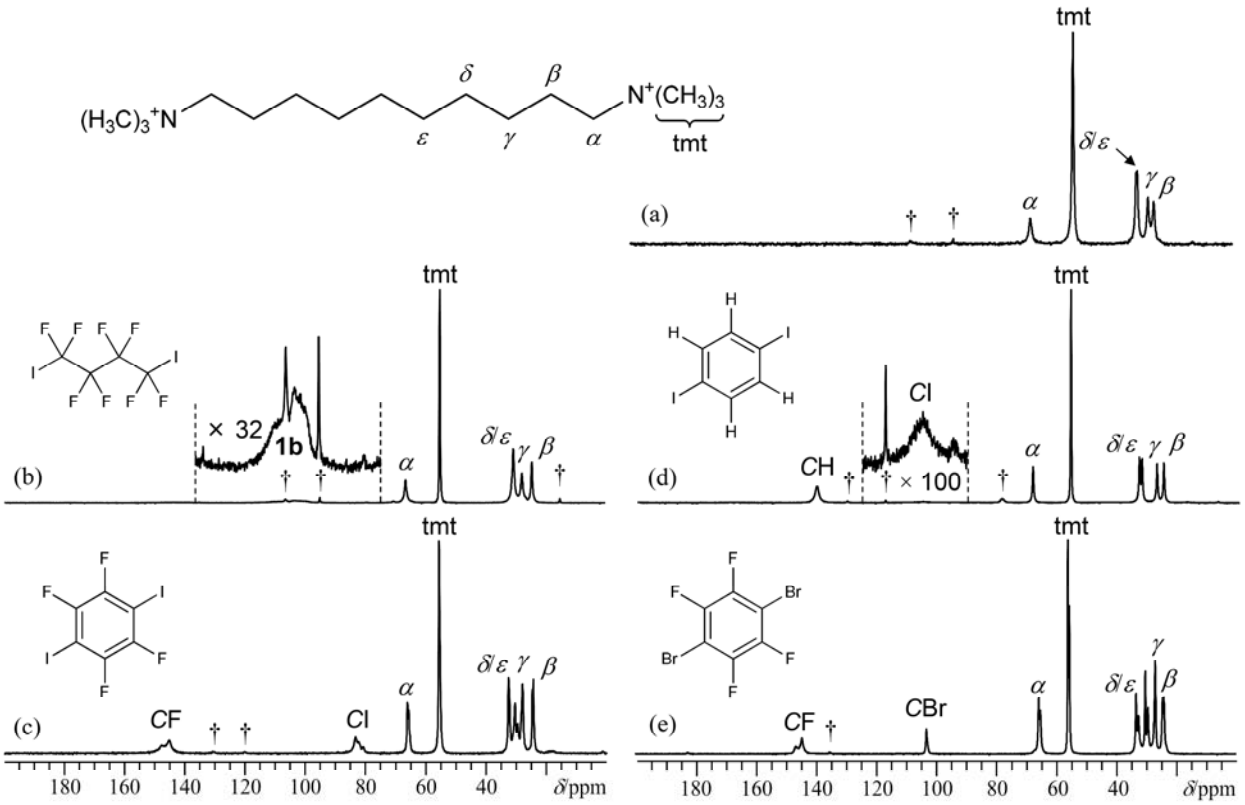

Figure S4. Experimental ^{13}C RAMP-CP/MAS NMR spectra of compounds **1a·2H$_2$O** (a), **P1** (b), **P2** (c), **P3** (d), and **P4** (e). All complexes include the decamethonium dication (i.e., $(CH_3)_3N^+(CH_2)_{10}N^+(CH_3)_3$) within their respective structures. The spectra in (a, b, and e) were acquired at B_0 = 11.75 T and ν_{MAS} = 5 – 10 kHz, while the spectra in (c) and (d) were acquired at B_0 = 9.4 T, and using ν_{MAS} = 6.5 and 6.2 kHz, respectively. All spectra were obtained at T = 285 K, expect for (e), which was performed at room temperature. Minor peaks due to MAS spinning sidebands are denoted using a dagger. Note that, for (b) and (d) the spectral regions within the dashed lines have been increased by the factors indicated in order to better illustrate the broad signals that are associated with carbon atoms bound to an iodine atom. The labeling scheme used for the alkyl chain is indicated in the inset to (a). Note that for **P1** in (b), the individual carbon sites associated with the **1b** molecule could not be resolved from one another.

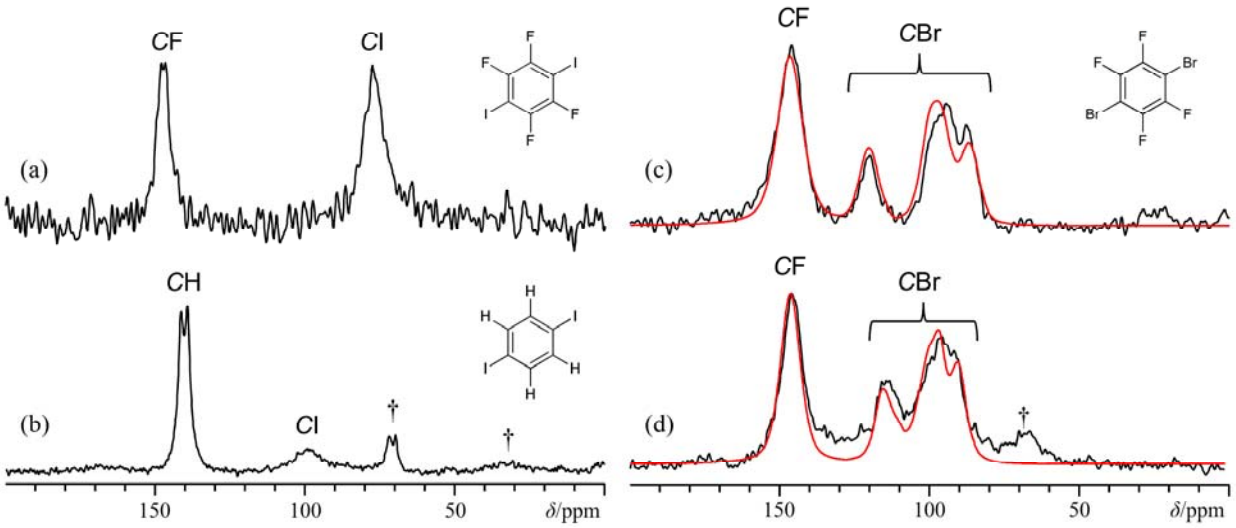

Figure S5. Experimental direct detection ^{13}C NMR spectra of compounds **2b** (a), and **4b** (c, d; black traces), and RAMP-CP/MAS NMR spectrum of compound **3b** (b). All experimental spectra were acquired at B_0 = 9.4 T and T = 285 K, except for (d), which was acquired at B_0 = 11.75 T and T = room temperature. Minor peaks due to MAS spinning sidebands are denoted using a dagger. A very detailed account of the line shape generation procedure for the simulated line shapes (i.e., the red traces in (c) and (d)) is provided in the additional experimental section. Parameters used for the simulations: $C_Q(^{79}Br)$ = −599 MHz; $C_Q(^{81}Br)$ = −501 MHz; η_Q = 0.11; δ_{iso} = 100.5 ppm; $D_{eff}(^{13}C\text{-}^{79}Br)$ = 1097 Hz; $D_{eff}(^{13}C\text{-}^{81}Br)$ = 1183 Hz; $J_{iso}(^{13}C\text{-}^{79}Br)$ = −216 Hz; $J_{iso}(^{13}C\text{-}^{81}Br)$ = −233 Hz; $\Delta J(^{13}C\text{-}^{79}Br)$ = 130.5 Hz; $\Delta J(^{13}C\text{-}^{81}Br)$ = 140.7 Hz; $\alpha_{RDC} = \beta_{RDC} = 0°$.

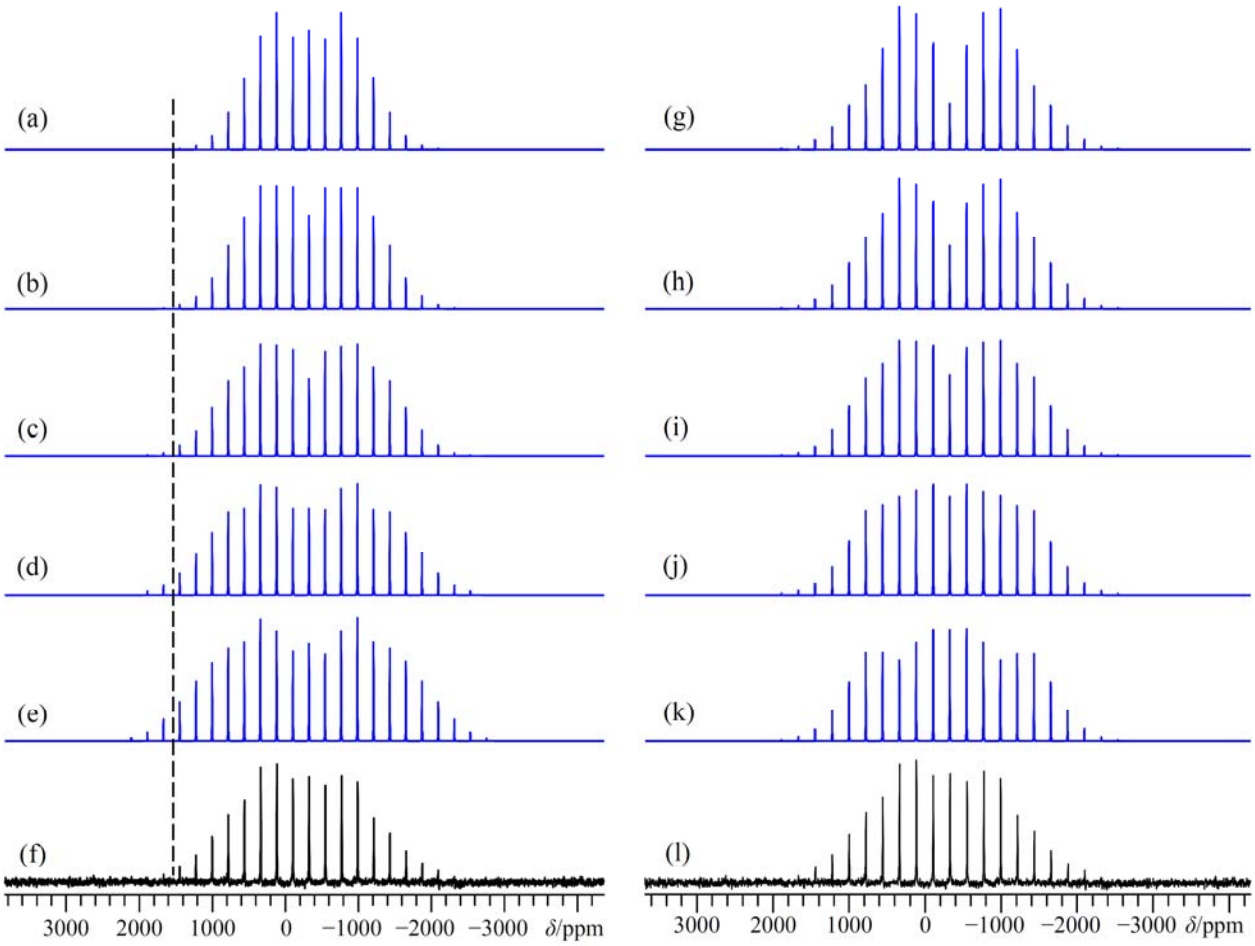

Figure S6. Numerical SIMPSON simulations (a-e; g-k), and experimental VOCS ^{14}N MAS NMR spectrum (f, l) of **1a·2H$_2$O** intending to highlight the rough data fit for this system, as denoted in the main text. For the simulation traces in the left-hand column, the value for $C_Q(^{14}N)$ is varied (while $\eta_Q = 0.45$): (a) $C_Q = 65$ kHz; (b) $C_Q = 75$ kHz; (c) $C_Q = 85$ kHz; (d) $C_Q = 95$ kHz; (e) $C_Q = 105$ kHz. The best fit to the experimental data in (f) leads to a C_Q of roughly 85 kHz. The dashed line highlights the small changes which occur in the breadth of the spectrum as a function of the C_Q values. For the simulation traces in the right-hand column, the value for η_Q is varied ($C_Q = 85$ kHz): (g) $\eta_Q = 0.25$; (h) $\eta_Q = 0.35$; (i) $\eta_Q = 0.45$; (j) $\eta_Q = 0.55$; (k) $\eta_Q = 0.65$. The best fit to the experimental data in (l) is for roughly $\eta_Q = 0.5$. For all spectra $\nu_{MAS} = 8$ kHz, and for (f, l) $T = 285$ K.

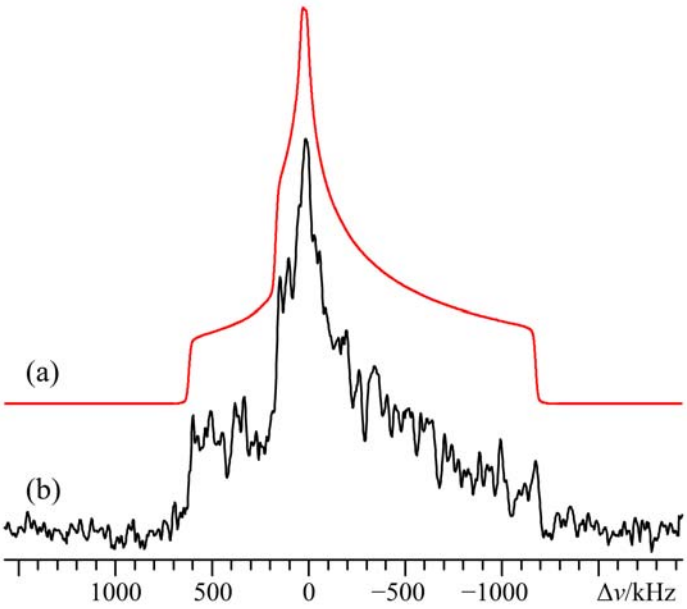

Figure S7. Analytical WSolids simulation (a), and experimental VOCS Solomon echo ^{127}I NMR spectrum of the **1a·2H$_2$O** starting material (b), acquired at B_0 = 9.4 T. The line shape generated in (a) uses the parameters established from ^{127}I SSNMR data at 21.1 T and hence illustrates that while the two datasets are consistent, we are nevertheless unable to extract chemical shift anisotropy information, as the data acquired at the lower field are not of high enough quality.

Table S7. GIPAW DFT quantum chemical H atom geometry optimizations – pseudopotential files used, energies and structure references[a]

compound	pseudopotential files used	energy / eV	structure reference(s) and additional details[b]
1a · 2H$_2$O	H_00PBE.usp; C_00PBE.usp; N_00PBE.usp; O_00PBE.usp; I_00PBE.usp	−5201.397375	Metrangolo *et al*.[35] Optimization used 'standard' setting for FFT grid; E_{cut} = 800 eV; 3 × 3 × 3 *k*-point grid (14 *k*-points)
3b	H_00PBE.usp; C_00PBE.usp; I_00PBE.usp	−6475.694766	Boese and Mierbach.[36] Standard FFT grid; E_{cut} = 800 eV; 1 × 3 × 4 *k*-point grid (6 *k*-points)
P3	H_00PBE.usp; C_00PBE.usp; N_00PBE.usp; I_00PBE.usp	−11763.649368	Present study. Standard FFT grid; E_{cut} = 800 eV; 1 × 3 × 3 *k*-point grid (5 *k*-points)
P5	H_00PBE.usp; C_00PBE.usp; N_00PBE.usp; I_00PBE.usp	−8280.300811	Abate *et al*.[37] Standard FFT grid; E_{cut} = 800 eV; 1 × 3 × 3 *k*-point grid (5 *k*-points)

[a] All GIPAW DFT geometry optimizations used the PBE XC functional,[38, 39] as described in the main text. Optimized structure parameters can be found in Table S10.
[b] E_{cut} = plane wave basis set energy cut-off. Basis set convergence was tested and ensured for all systems.

Table S8. GIPAW DFT magnetic shielding and EFG tensor calculations – pseudopotential files used, energies and structure references[a]

compound	pseudopotential files used	energy / eV	additional details
1a · 2H$_2$O	H_00.otfg; C_00.otfg; N_00.otfg; O_00.otfg; I_00.otfg	−5960.228092	E_{cut} = 800 eV; 3 × 3 × 3 *k*-point grid (14 *k*-points)
P3	H_00.otfg; C_00.otfg; N_00.otfg; I_00.otfg	−14732.005647	E_{cut} = 800 eV; 1 × 3 × 3 *k*-point grid (5 *k*-points)
P5	H_00.otfg; C_00.otfg; N_00.otfg; I_00.otfg	−11196.227254	E_{cut} = 800 eV; 1 × 3 × 3 *k*-point grid (5 *k*-points)

[a] All GIPAW DFT computations of EFG and magnetic shielding tensor parameters used the PBE XC functional, as described in the main text. Full details of the computed parameters are in Table S9. Information on the iodine otfg pseudopotential: (i) core states include $1s^2 2s^2 2p^6 3s^2 3p^6 3d^{10} 4s^2 4p^6 4d^{10}$; valence states include $5s^2 5p^5$; (ii) the local channel is chosen to be *d*; (iii) the pseudisation radius for local and non-local channels is 2.0 a.u.; (iv) the pseudisation radius for augmentation functions is 1.6 a.u.; (v) augmentation charge and partial core correction are 1.602 a.u.; (vi) the string used for the generation of the pseudopotential, in the format used by Materials Studio is "2|2|2|1.6|6|7.3|9.9|50U=-0.65U=+0:51U=-0.265U=+0[]"
(see **http://www.tcm.phy.cam.ac.uk/castep/usp-string-notes.txt** and **http://www.tcm.phy.cam.ac.uk/castep/otfg.pdf** for further explanation).

Table S9. GIPAW DFT-computed nitrogen and iodine EFG and magnetic shielding tensor parameters – additional information[a]

nucleus	site label	V_{11} / a.u.	V_{22} / a.u.	V_{33} / a.u.	C_Q(X) / MHz	η_Q	σ_{11} / ppm	σ_{22} / ppm	σ_{33} / ppm	Ω / ppm	κ	δ_{iso}[b] / ppm
1a·2H$_2$O												
$^{14/15}$N	—	0.0079	0.0184	−0.0263	−0.1263	0.402	161.47	166.53	178.84	17.37	0.417	—
^{127}I	—	0.0092	0.4931	−0.5024	82.16	0.963	4751.18	4889.25	4926.70	175.52	−0.573	181.79
P3												
$^{14/15}$N	—	0.0016	0.0175	−0.0191	−0.0917	0.833	160.03	164.22	175.55	15.52	0.460	—
^{127}I	2	−0.3968	−0.6708	1.0677	−174.61	0.257	4438.95	4481.56	4918.41	479.46	0.822	425.76
	1	−4.8612	−6.0163	10.8774	−1778.84	0.106	2496.92	2713.92	4936.37	2439.45	0.822	1662.56
P5												
$^{14/15}$N	—	0.0033	0.0199	−0.0233	−0.1119	0.715	153.95	165.68	172.05	18.10	−0.296	—
^{127}I	1	−1.0507	−1.5089	2.5597	−418.60	0.179	3672.02	3706.62	4937.09	1265.07	0.945	936.06
	2	−5.5441	−6.2994	11.8435	−1936.83	0.064	2700.59	2730.79	5406.83	2706.24	0.978	1431.06

[a] $Q(^{14}N) = 2.044 \times 10^{-30}$ m^2; $Q(^{127}I) = -6.96 \times 10^{-29}$ m^2.[40] To convert $V_{33}(^{14}N)$ and $V_{33}(^{127}I)$ into frequency units, conversion factors of 4.80268 MHz/a.u. and −163.53549 MHz/a.u. were used for ^{14}N and ^{127}I, respectively, and the unit EFG is $9.71736166 \times 10^{21}$ J C^{-1} m^{-2}.

[b] For iodine only, to map quantum chemical calculations of magnetic shielding values into chemical shifts, the following procedure was used: (i) using E_{cut} = 1000 eV and a 6 × 6 × 6 *k*-points, the iodine magnetic shielding in solid NaI was calculated as 4811.02 ppm; (ii) knowing experimentally that this shielding value corresponds to a shift of 226.71 ppm (relative to infinitely dilute $I^-(aq)$), the theoretical shielding of $I^-(aq)$ was calculated as 5036.59 ppm (using the familiar definition of the chemical shift: $\delta_{iso} = (\sigma_{iso,ref} - \sigma_{iso})/(1 - \sigma_{iso,ref})$, with δ_{iso} = 226.71 ppm and σ_{iso} = 4811.02 ppm); (iii) all other shift values were then calculated relative to this value of 5036.59 ppm for $\sigma_{iso,ref}$.

Table S10. Coordinates after H-optimization for GIPAW DFT quantum chemical computations[a]

atom	Wyckoff position	site symmetry	X[b]	Y[b]	Z[b]
1a·2H$_2$O[c]					
I1	2i	1	0.0566	0.6929	0.2587
O1	2i	1	0.2971	0.3026	0.4019
N1	2i	1	0.7874	0.2110	0.3068
C1	2i	1	0.6885	0.3847	0.3246
C2	2i	1	0.7123	0.4951	0.1742
C3	2i	1	0.5887	0.6602	0.2004
C4	2i	1	0.6160	0.7785	0.0564
C5	2i	1	0.4831	0.9396	0.0700
C6	2i	1	0.9725	0.1924	0.2532
C7	2i	1	0.7304	0.1458	0.1937
C8	2i	1	0.7487	0.1182	0.4638
H1	2i	1	0.5546	0.3843	0.3702
H2	2i	1	0.7302	0.4209	0.4156
H3	2i	1	0.6913	0.4492	0.0765
H4	2i	1	0.8430	0.5062	0.1379
H5	2i	1	0.4567	0.6522	0.2306
H6	2i	1	0.6049	0.7045	0.3019
H7	2i	1	0.7433	0.7951	0.0367
H8	2i	1	0.6188	0.7270	−0.0491
H9	2i	1	0.3565	0.9226	0.0854
H10	2i	1	0.4750	0.9885	0.1788
H11	2i	1	1.0005	0.2554	0.1360
H12	2i	1	1.0385	0.0647	0.2475
H13	2i	1	1.0119	0.2420	0.3364
H14	2i	1	0.5917	0.1704	0.2322
H15	2i	1	0.7921	0.0168	0.1965
H16	2i	1	0.7697	0.2017	0.0745
H17	2i	1	0.6115	0.1327	0.5000
H18	2i	1	0.7885	0.1651	0.5490
H19	2i	1	0.8184	−0.0077	0.4509
H20	2i	1	0.2430	0.4051	0.3480
H21	2i	1	0.2097	0.2968	0.5020

atom	Wyckoff position	site symmetry	X[b]	Y[b]	Z[b]
3b[d]					
I	8c	1	0.6709	0.9600	0.1950
C1	8c	1	0.5682	0.9813	0.3810
C2	8c	1	0.4974	0.9286	0.2929
C3	8c	1	0.5716	0.0532	0.5893
H1	8c	1	0.4945	0.8717	0.1296
H2	8c	1	0.6272	0.0956	0.6613
P3[e]					
I1	4i	*m*	0.4112	0.0000	0.1631
I2	4i	*m*	0.3222	0.0000	−0.1801
N1	4i	*m*	0.1742	0.0000	0.6966
C1	4i	*m*	0.1244	0.0000	0.6365
C2	4i	*m*	0.1156	0.0000	0.4195
C3	4i	*m*	0.0644	0.0000	0.3780
C4	4i	*m*	0.0548	0.0000	0.1605
C5	4i	*m*	0.0044	0.0000	0.1084
C6	8j	1	0.1974	0.1661	0.6269
C7	4i	*m*	0.1768	0.0000	0.9140
C8	4i	*m*	0.4645	0.0000	0.3684
C9	4i	*m*	0.5095	0.0000	0.3047
C10	4i	*m*	0.4551	0.0000	0.5636
H1	8j	1	0.1095	0.1203	0.7052
H2	8j	1	0.1307	0.1202	0.3514
H3	8j	1	0.0486	0.1192	0.4453
H4	8j	1	0.0711	0.1193	0.0945
H5	8j	1	−0.0121	0.1189	0.1745
H6a	8j	1	0.1797	0.2840	0.6860
H6b	8j	1	0.1964	0.1717	0.4684
H6c	8j	1	0.2327	0.1622	0.6785
H7a	8j	1	0.1604	0.1224	0.9692
H7b	4i	*m*	0.2129	0.0000	0.9550
H9	4i	*m*	0.5174	0.0000	0.1505
H10	4i	*m*	0.4201	0.0000	0.6170
P5[f]					
I1	4i	*m*	0.1770	0.0000	0.3372

atom	Wyckoff position	site symmetry	X[b]	Y[b]	Z[b]
I2	4i	*m*	0.0513	0.0000	0.4491
N1	4i	*m*	0.3328	0.0000	0.0687
C1	4i	*m*	0.3781	0.0000	−0.0629
C2	4i	*m*	0.4311	0.0000	0.0859
C3	4i	*m*	0.4718	0.0000	−0.0733
C4	8j	1	0.3327	0.1616	0.2161
C5	4i	*m*	0.2836	0.0000	−0.1148
H1	8j	1	0.3724	0.1186	−0.1740
H2	8j	1	0.4370	0.1177	0.1988
H3	8j	1	0.4669	0.1178	−0.1864
H4	8j	1	0.3672	0.1617	0.3538
H5	8j	1	0.3331	0.2789	0.1059
H6	8j	1	0.2972	0.1593	0.2936
H7	4j	*m*	0.2497	0.0000	−0.0260
H8	8j	1	0.2838	0.1193	−0.2214

[a] All hydrogen atomic positions have been geometry optimized.
[b]. Values in these columns are in fractional unit cell units.
[c] Original structure (i.e., non H-optimized) obtained from the Cambridge crystallographic database (CCSD), version 5.33 (Nov. 11). CCSD identity code: XOVBIU. $P\bar{1}$; a = 8.534 Å; b = 8.858 Å; c = 8.891 Å; α = 80.00°; β = 73.486°; γ = 71.754°; V = 609.33 Å^3; Z = 1.
[d] Original structure obtained from the CCSD. CCSD identity code: ZZZPRO05. *Pbca*; a = 16.9697 Å; b = 7.3242 Å; c = 6.156 Å; $\alpha = \beta = \gamma$ = 90°; V = 765.13 Å^3; Z = 4.
[e] Original structure obtained from this study. *C*2/*m*; a = 29.382 Å; b = 7.4019 Å; c = 6.8939 Å; α = 90°; β = 90.113°; γ = 90°; V = 1499.30 Å^3; Z = 4.
[f] Original structure obtained from the CCSD. CCSD identity code: NUTSOL. *C*2/*m*; a = 25.963 Å; b = 7.5588 Å; c = 5.8260 Å; α = 90°; β = 100.17°; γ = 90°; V = 1125.38 Å^3; Z = 4.

Table S11. Cartesian coordinates after ADF DFT optimization for molecular compounds[a]

Atom	*x* / Å	*y* / Å	*z* / Å
p-dibromobenzene; bond energy = −81.37577 eV			
C	−1.24599	0.84330	0.00008
C	0.14689	0.82829	0.00052
C	0.84434	2.03616	−0.00001
C	0.13504	3.23501	−0.00097
C	−1.25784	3.25002	−0.00141
C	−1.95530	2.04214	−0.00088
H	−1.79750	4.18909	−0.00215
H	−3.03851	2.04009	−0.00121
H	1.92674	2.03823	0.00032
H	0.68632	−0.11042	0.00127
Br	1.08925	4.88754	−0.00170
Br	−2.20019	−0.80923	0.00081
4b; bond energy = −81.46053 eV			
C	−1.25951	0.82003	0.00009
C	0.13483	0.83689	0.00056
C	0.83084	2.04230	0.00002
C	0.14840	3.25833	−0.00098
C	−1.24593	3.24146	−0.00145
C	−1.94194	2.03605	−0.00091
F	−1.94038	4.38908	−0.00241
F	−3.28303	2.06372	−0.00138
F	2.17193	2.01463	0.00050
F	0.82928	−0.31072	0.00152
Br	1.08894	4.88710	−0.00170
Br	−2.20018	−0.80867	0.00081

[a] Calculations were performed as part of the additional discussion of the residual dipolar coupling observed in the ^{13}C NMR spectra in Figure S5.

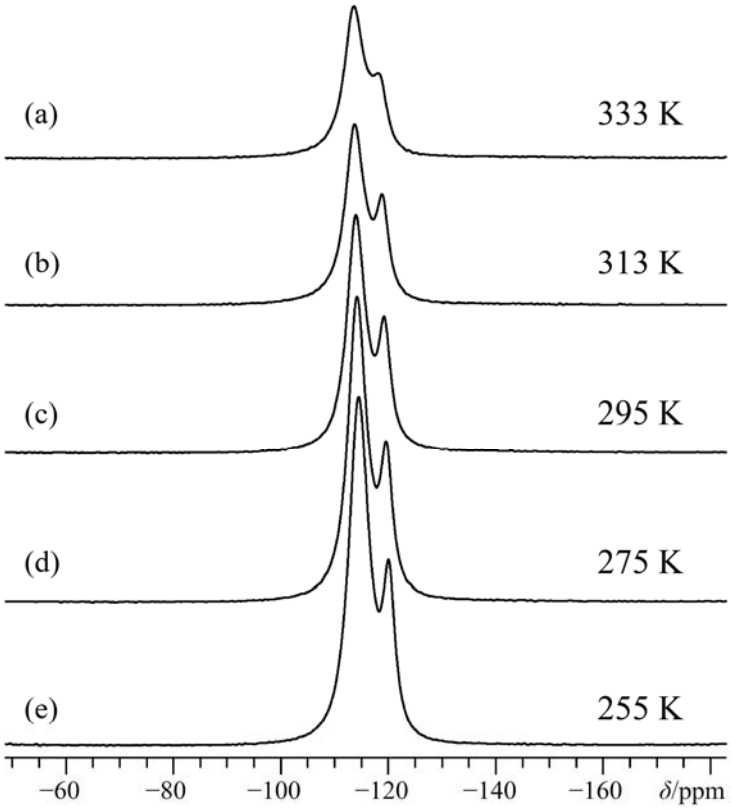

Figure S8. Experimental ^{19}F Hahn echo MAS NMR spectra of sample **P2**, which demonstrate the minimal changes in the ^{19}F NMR spectrum as a function of the temperatures shown. For all experiments, ν_{MAS} = 15.0 kHz.

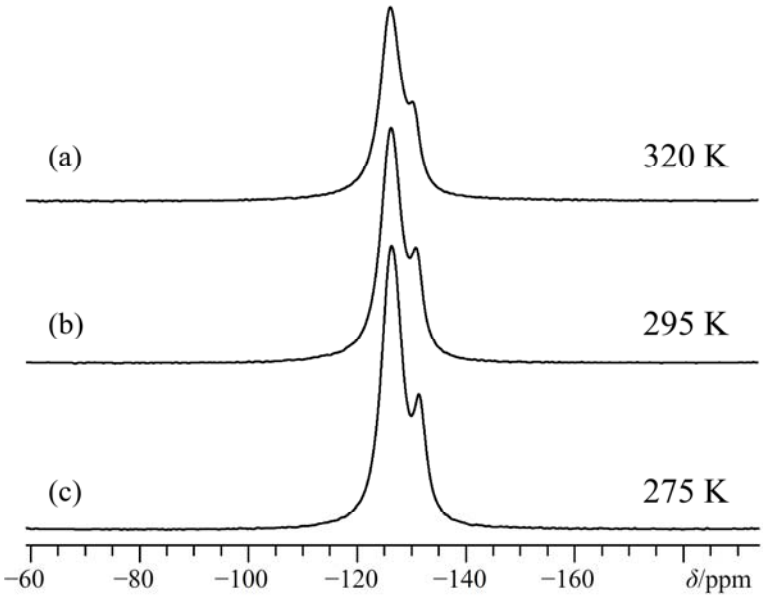

Figure S9. Experimental ^{19}F Hahn echo MAS NMR spectra of sample **P4**, which demonstrate the minimal changes in the ^{19}F NMR spectrum as a function of the temperatures shown. For all experiments, ν_{MAS} = 15.0 kHz.

References

[1] M. C. Burla, M. Camalli, B. Carrozzini, G. L. Cascarano, C. Giacovazzo, G. Polidori, R. Spagna *J. Appl. Cryst.* **2003***, 36*, 1103.

[2] G. M. Sheldrick *Acta Cryst. A* **2008***, A64*, 112-122.

[3] D. Massiot, I. Farnan, N. Gautier, D. Trumeau, A. Trokiner, J. P. Coutures *Solid State Nucl. Magn. Reson.* **1995***, 4*, 241-248.

[4] A. Medek, V. Frydman, L. Frydman *J. Phys. Chem. A* **1999***, 103*, 4830-4835.

[5] R. W. Schurko, S. Wi, L. Frydman *J. Phys. Chem. A* **2002***, 106*, 51-62.

[6] M. Bak, J. T. Rasmussen, N. C. Nielsen *J. Magn. Reson.* **2000***, 147*, 296.

[7] V. V. Terskikh, S. J. Lang, P. G. Gordon, G. D. Enright, J. A. Ripmeester *Magn. Reson. Chem.* **2009***, 47*, 398-406.

[8] D. L. Bryce, *Tensor Interplay* in NMR Crystallography. John Wiley & Sons, West Sussex, United Kingdom, **2009**, pp. 289-301.

[9] S. Kojima, K. Tsukada, Y. Hinaga *J. Phys. Soc. Jpn.* **1955***, 10*, 498-502.

[10] K. Shimomura *J. Phys. Soc. Jpn.* **1959***, 14*, 235-236.

[11] P. Bucci, P. Cecchi, A. Colligiani *J. Am. Chem. Soc.* **1964***, 86*, 2513-2514.

[12] G. te Velde, F. M. Bickelhaupt, E. J. Baerends, C. F. Guerra, van Gisbergen, S. J. A., J. G. Snijders, T. Ziegler *J. Comp. Chem.* **2001**, *22*, 931-937.

[13] C. Fonseca Guerra, J. G. Snijders, G. te Velde, E. J. Baerends *Theor. Chem. Acc.* **1998**, *99*, 391-403.

[14] SCM, Theoretical Chemistry, Vrije Universiteit, Amsterdam, The Netherlands, ADF v. 2012.01. http://www.scm.com.

[15] E. van Lenthe, J. G. Snijders, E. J. Baerends *J. Chem. Phys.* **1996**, *105*, 6505-6516.

[16] J. Tao, J. P. Perdew, V. N. Staroverov, G. E. Scuseria *Phys. Rev. Lett.* **2003**, *91*, 146401.

[17] V. N. Staroverov, G. E. Scuseria, J. Tao, J. P. Perdew *J. Chem. Phys.* **2003**, *119*, 12129-12137.

[18] J. P. Perdew, A. Ruzsinszky, J. Tao, V. N. Staroverov, G. E. Scuseria *J. Chem. Phys.* **2005**, *123*, 062201.

[19] F. A. Perras, D. L. Bryce *J. Chem. Phys.* **2013**, *138*, 174202.

[20] A. Maiga, Nguyen-ba-Chanh, Y. Haget, M. A. Cuevas-Diarte *J. Appl. Cryst.* **1984**, *17*, 210-211.

[21] G. S. Pawley, G. A. Mackenzie, O. W. Dietrich *Acta. Cryst. A* **1977**, *A33*, 142-145.

[22] R. M. Dickson, T. Ziegler *J. Phys. Chem.* **1996**, *100*, 5286-5290.

[23] J. Khandogin, T. Ziegler *Spectrochim. Acta A* **1999**, *55*, 607-624.

[24] J. Autschbach, T. Ziegler *J. Chem. Phys.* **2000**, *113*, 936-947.

[25] J. Autschbach, T. Ziegler *J. Chem. Phys.* **2000**, *113*, 9410-9418.

[26] J. Autschbach *J. Chem. Phys.* **2008**, *129*, 094105.

[27] J. Autschbach *J. Chem. Phys.* **2008**, *128*, 164112.

[28] J. Autschbach *ChemPhysChem* **2009**, *10*, 2274-2283.

[29] D. L. Bryce, J. Autschbach *Can. J. Chem.* **2009**, *87*, 927-941.

[30] M. Salvador, J. Autschbach *J. Chem. Theor. Comput.* **2010**, *6*, 223-234.

[31] B. M. Fung, A. K. Khitrin, K. Ermolaev *J. Magn. Reson.* **2000**, *142*, 97-101.

[32] A. E. Bennett, C. M. Rienstra, M. Auger, K. V. Lakshmi, R. G. Griffin *J. Chem. Phys.* **1995**, *103*, 6951-6958.

[33] I. Solomon *Phys. Rev.* **1958**, *110*, 61-65.

[34] E. L. Hahn *Phys. Rev.* **1950**, *80*, 580-594.

[35] P. Metrangolo, Y. Carcenac, M. Lahtinen, T. Pilati, K. Rissanen, A. Vij, G. Resnati *Science* **2009**, *323*, 1461-1464.

[36] R. Boese, T. Miebach, CCDC ID code: ZZZPRO05.

[37] A. Abate, M. Brischetto, G. Cavallo, M. Lahtinen, P. Metrangolo, T. Pilati, S. Radice, G. Resnati, K. Rissanen, G. Terraneo *Chem. Commun.* **2010***, 46*, 2724-2726.

[38] J. P. Perdew, K. Burke, M. Ernzerhof *Phys. Rev. Lett.* **1996***, 77*, 3865-3868.

[39] J. P. Perdew, K. Burke, M. Ernzerhof *Phys. Rev. Lett.* **1997***, 78*, 1396.

[40] P. Pyykkö *Mol. Phys.* **2008***, 106*, 1965-1974.